Sub-7-femtosecond conical-intersection dynamics probed at the carbon K-edge

Journal Article

Author(s):
Zinchenko, Kristina S.; Ardana-Lamas, Fernando; Seidu, Issaka; Neville, Simon P.; van der Veen, Joscelyn; Lanfaloni, Valentina Utrio; Schuurman, Michael S.; Wörner, Hans Jakob

Sub-7-femtosecond conical-intersection dynamics probed at the carbon K-edge

Kristina S. Zinchenko[1,*], Fernando Ardana-Lamas[1,*,†], Issaka Seidu[2,*],
Simon P. Neville[2,*], Joscelyn van der Veen[2,*], Valentina Utrio Lanfaloni[1],
Michael S. Schuurman[2,‡], Hans Jakob Wörner[1,‡]

[1] Laboratorium für Physikalische Chemie, ETH Zürich, 8093 Zürich, Switzerland

[2] National Research Council of Canada, Ottawa, Canada

[*] These authors contributed equally to this work

[†] Present Address: European XFEL GmbH, Schenefeld, Germany

[‡] **E-mails: michael.schuurman@nrc-cnrc.gc.ca, hwoerner@ethz.ch**

Conical intersections allow electronically excited molecules to return to their electronic ground state. Here, we observe the fastest electronic relaxation dynamics measured to date by extending attosecond transient-absorption spectroscopy (ATAS) to the carbon K-edge. We selectively launch wave packets in the two lowest electronic states (D_0 and D_1) of $C_2H_4^+$. The electronic $D_1 \rightarrow D_0$ relaxation takes place with a short time constant of 6.8 ± 0.2 fs. The electronic-state switching is directly visualized in ATAS owing to a spectral separation of the D_1 and D_0 bands caused by electron correlation. Multidimensional structural dynamics of the molecule are simultaneously observed. Our results demonstrate the capability to resolve the fastest electronic and structural dynamics in the broad class of organic molecules. They show that electronic relaxation in the prototypical organic chromophore can take place within less than a single vibrational period.

Electronically excited molecules can decay through a variety of channels, including fluorescence, bond dissociation, or nonradiative electronic relaxation to lower-lying states. The key in defining the relative importance of these decay channels are the associated time scales. Electronic relaxation is known to be particularly fast when mediated by conical intersections (*1,2*), enabling the photostability of DNA bases (*3*), the remarkable quantum yield of retinal isomerization in vision (*4, 5*) and the efficiency of charge separation in organic semiconductors (*6*).

But how fast electronic relaxation really is has remained elusive in many molecular systems, owing to experimental limitations, particularly temporal resolution. This situation has changed with the advent of attosecond science that has redefined the frontiers of time-resolved measurements on molecules (*7–14*). Attosecond transient-absorption spectroscopy (ATAS) is a particularly powerful technique for accessing both electronic and structural dynamics (*15–21*). With respect to dynamics at conical intersections (*22*), the methods of attosecond science provide the ultimate time resolution that is required to unambiguously monitor and dissect the intimately coupled electronic and nuclear dynamics that take place in their vicinity. Pioneering ATAS work in the extreme-ultraviolet domain has followed curve-crossing dynamics in diatomic molecules (*20*) and monitored dynamics induced by conical intersections through the appearance time of atomic fragments (*23*).

Here, we demonstrated ATAS at the carbon K-edge, which extends its applicability from systems containing specific reporter atoms to the general class of organic molecules. We studied ethylene as the most important organic chromophore involved in the photochemistry and photophysics of a majority of molecular systems (*24–32*). Rather than using one-photon excitation as in typical femtochemistry experiments, we used a carrier-envelope-phase (CEP) stable sub-two-cycle pulse (*33*) to prepare the first electronically excited state (D_1) of $C_2H_4^+$ and probed its relaxation to the electronic ground state (D_0) using transient absorption of an attosecond soft-X-ray continuum covering the carbon K-edge. The experimental results were compared with *ab-initio* multiple-spawning (AIMS) quantum dynamics simulations (*34*) coupled to X-ray absorption calculations (*35,36*). This technique

2

has the distinctive advantage that it does neither require any assumptions regarding the dynamics nor precomputed potential-energy surfaces and is thus truly predictive. The recent extension of the combined density-functional theory and multireference configuration-interaction (DFT/MRCI) method to calculate transient X-ray spectra on the fly (*37*) was validated here against experimental data. The strong-field-ionization step is described using the time-dependent first-order algebraic diagrammatic construction (TD-ADC(1)) method, including the complete state-specific molecular-orientation dependence of the strong-field ionization rates.

This joint experimental and theoretical study provided a comprehensive view of the coupled electronic and nuclear dynamics of the ethylene cation. The structural dynamics driven by the vibrational wave packet in the D_0 state was identified through its modulation of the line positions in both pre-edge and post-edge transitions. These spectral fingerprints simultaneously revealed the electronic character of the involved core-level transitions and the electronically adiabatic structural dynamics occurring in the ionized molecule. The non-adiabatically coupled electronic and nuclear wave packet prepared in the D_1 state was found to electronically relax with a fast time constant of 6.8 ± 0.2 fs, representing the fastest electronic relaxation measured to date.

These results demonstrate the potential of ATAS at the carbon K-edge to resolve the fastest chemical processes in the general class of organic molecules (*38, 39*). They moreover demonstrate the existence of electronic relaxation on time scales far below vibrational periods, which is likely to be a general phenomenon of relevance to the photochemistry and photophysics of most molecular systems.

The experimental setup is schematically illustrated in Fig. 1**A**, with details given in the Supplementary Material (SM, Section S1). Strong-field ionization of ethylene was initiated by a passively CEP-stable sub-two-cycle (10.4 ± 1.5 fs) laser pulse centered at 1.6 μm. Transient-absorption spectra were acquired by measuring the transmission of an X-ray supercontinuum extending to above 450 eV (with an estimated sub-200-as duration), thus covering the carbon K-edge with a nearly constant photon flux (Fig. S2). In this experiment, the time resolution is thus limited by the pump pulse.
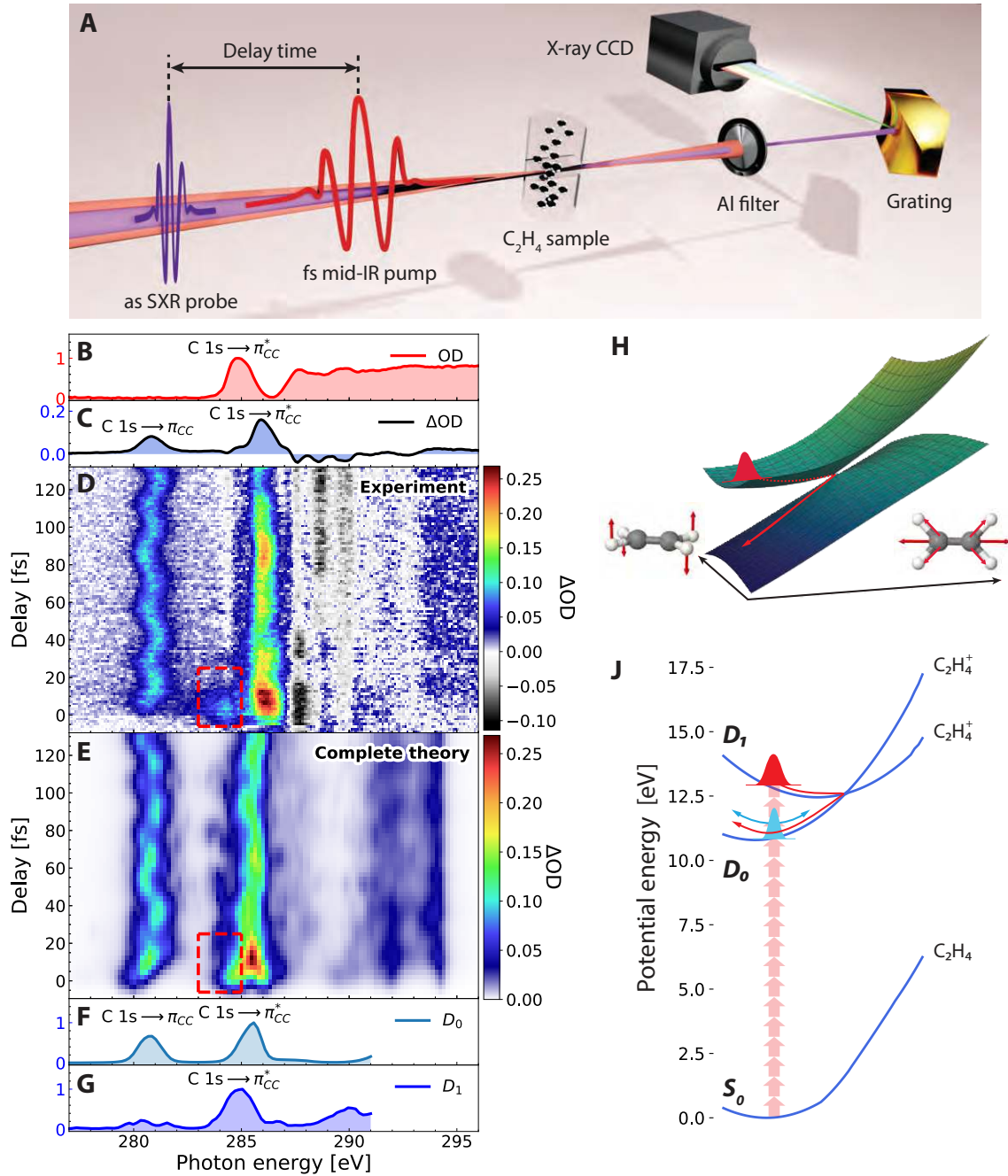
Figure 1: **Attosecond transient-absorption spectroscopy of ethylene at the carbon K-edge** (**A**) Experimental setup. (**B**) Overview of measured data showing the optical density (OD) of the unexcited target and (**C**) its change under the action of the pump pulse (ΔOD). (**D**) Experimental and (**E**) calculated (complete simulation) ΔOD as a function of pump-probe delay. The bottom panels show the calculated X-ray absorption spectrum of $C_2H_4^+$ in its electronic ground (D_0) (**F**), and excited state (D_1) (**G**). (**H,J**) Illustration of the conical intersection between the D_1 and D_0 states of $C_2H_4^+$ mediating the electronic relaxation.

4

Figure 1**B** shows the experimental X-ray absorption spectrum of neutral ethylene in its electronic ground state (S_0). It is dominated by the C1s$\rightarrow \pi^*$ transition, followed by two weaker excitations and the onset of continuum absorption (see also Fig. S3). The change in optical density induced by the pump pulse (ΔOD) is shown in Fig. 1**C**, obtained by integrating the transient data over time delays longer than 20 fs. This spectrum is characterized by the appearance of an additional absorption band at 281 eV, corresponding to the 1s$\rightarrow \pi$ transition into the singly-occupied π molecular orbital and a shift of the 1s$\rightarrow \pi^*$ transition to higher energies.

Figure 1**D** shows ΔOD as a function of the pump-probe delay, where a positive delay means that the mid-infrared (mid-IR) pulse preceded the soft-X-ray (SXR) pulse. The transient spectra are dominated by the 1s$\rightarrow \pi$ band centered at 281 eV that undergoes a periodic oscillation of its central position and the 1s$\rightarrow \pi^*$ band at 286 eV. Both bands are characteristic of the D_0 state, as revealed by comparison with the calculated spectrum shown in Fig. 1**F**. The oscillations of the band positions revealed the detailed structural dynamics in the D_0 state and are further discussed below.

The most remarkable feature in Fig. 1**D** is a short-lived transient centered at 284 eV (dashed red box). This feature was assigned to the D_1 state through comparison with the calculated spectrum in Fig. 1**G** and the detailed time-resolved calculations shown in Fig. 1**E**.

The experimental results are in excellent agreement with the calculations described above. Details on the theoretical methods are given in Section S3. Figure 1**F** and 1**G** show the transient spectra of the D_0 and D_1 electronic states of $C_2H_4^+$. They were obtained by integrating the transient spectra shown in 1**E** over pump-probe delays longer than 21.6 fs or from -9.6 to 21.6 fs, respectively.

These results enabled us to draw a comprehensive picture of the prepared dynamics (Figs. 1**H** and 1**J**). Strong-field ionization prepares coupled electronic and nuclear wave packets in both the D_0 and the D_1 states. The wave packet prepared in D_1 undergoes a fast electronic relaxation through a planar conical intersection accessed via stretching of the C=C bond. This dynamics is gradient directed (i.e., ballistic) and involves points of electronic degeneracy that lie close to the nuclear configurations

on the cationic excited state. Whereas earlier calculations (*40, 41*) and less direct measurements (*41*) qualitatively agree with our results, they associated time scales of 30-60 fs to the $D_1 \rightarrow D_0$ electronic relaxation. Both our measurements and our calculations showed that the process is much faster in reality. As we further detail below, the electronic relaxation was both extremely rapid and exceptionally efficient, occurring in less than a single C=C stretch vibrational period (22.4 fs (*42*)). Details of the dynamical simulations are presented in Sections S3 and S4.

The ultrafast decay of the characteristic D_1 absorption band was further analyzed in Fig. 2. Figure 2**A** shows the contribution of all 24 AIMS trajectory basis functions initiated in the D_1 state to the transient spectra. The dominant (1s$\rightarrow \pi^*$) absorption band centered at 284-285 eV decays on an ultrashort time scale. Figure 2**B** compares the measured ΔOD signal (blue dots) integrated over the spectral width of the D_1 band (red boxes in Figs. 1**D,E**) with the calculated spectra (orange crosses). A bi-exponential fit to the experimental data (full line) yielded time constants of 6.8$\pm$0.2 fs and 80.9$\pm$4.5 fs. The bi-exponential fit (dashed line) of the theoretical data was in excellent agreement with the short time constant (7.9$\pm$0.1 fs) and in reasonable agreement with the longer time constant (63.0$\pm$0.1 fs). The small differences in the time scales were attributed to the approximation of the initial phase-space distribution of the D_1 wave packet with that of the S_0 ground state. The statistical analysis of the results is shown in Figs. S4 and S5.

Figure 2**C** shows static X-ray-absorption spectra calculated at the equilibrium geometry of the neutral molecule (Franck-Condon (FC) point) for the D_1 state of $C_2H_4^+$, and at the geometry of the minimum-energy conical intersection (MECI) for both the D_1 and D_0 states. These static absorption spectra were calculated for a randomly oriented sample of ethylene, whereas the anisotropic axis distribution induced by strong-field ionization was included in the dynamic calculations (Fig. 2**A** and Section S4). The comparison of Figs. 2**A** and 2**C** showed that the shift of the D_1 band towards higher photon energies was the signature of wave-packet motion from the FC point to the MECI.

Interestingly, the calculations revealed a sudden shift of this band by >1 eV as the electronic
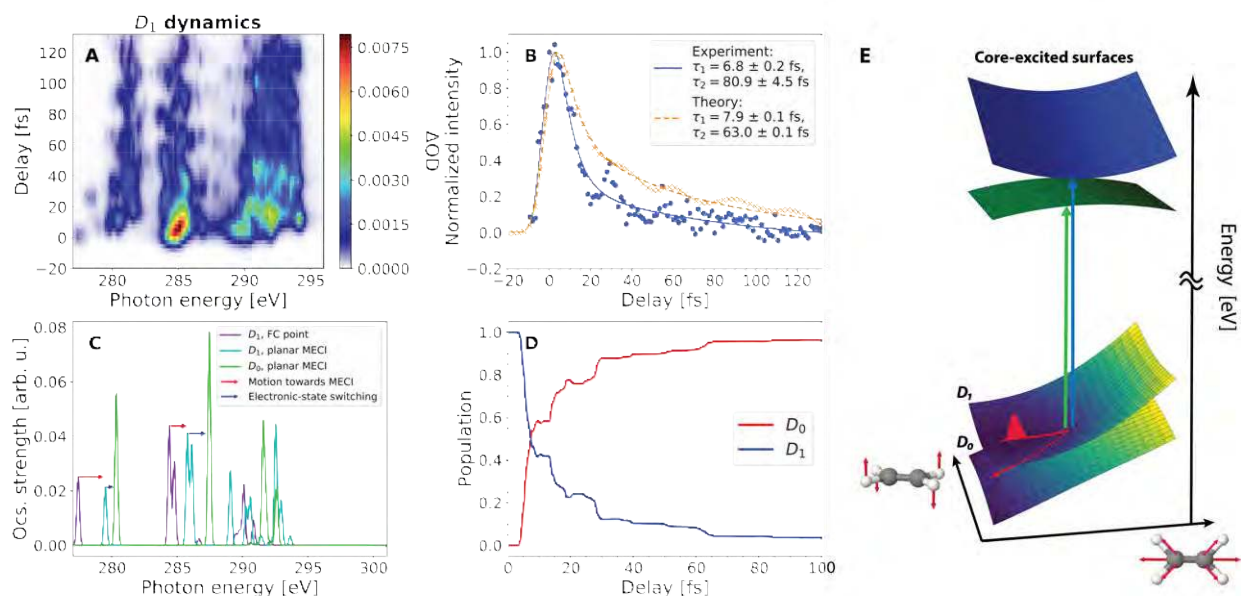
6

Figure 2: **Electronic relaxation probed by carbon K-edge ATAS**. (**A**) The calculated ΔOD contributions from AIMS simulations in which trajectories were initialized on the D_1 electronic state. (**B**) The evolution of the experimental and calculated (from **A**) ΔOD with pump-probe delay, integrated over the band centered at 284-285 eV. (**C**) Calculated XAS for geometries and electronic states of interest. All calculations were performed at the CVS-DFT/MRCI/aug-cc-pVDZ level of theory. (**D**) Adiabatic state populations from AIMS simulations in which trajectory basis functions were initialized on the D_1 electronic state. (**E**) Illustration of the mechanism resolving the electronic-state switching: The core-excited surfaces accessed from the D_0 and D_1 state (blue and green, respectively) are energetically separated at the location of the MECI between D_0 and D_1.
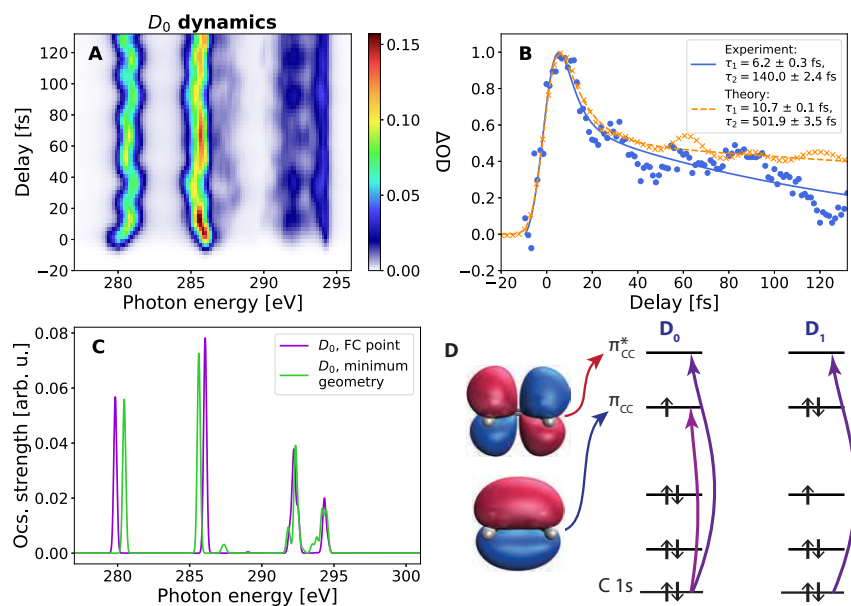
Figure 3: **Structural and electronic relaxation probed by carbon K-edge ATAS**. (**A**) Calculated ΔOD contributions from AIMS simulations in which trajectories were initialized on the D_0 electronic state. (**B**) The evolution of the experimental and calculated (from complete dynamics, Fig. 1**E**). (**C**) Calculated isotropic XAS for the D_0 state at both S_0 and D_0 minimum geometries. All calculations were performed at the CVS-DFT/MRCI/aug-cc-pVDZ level of theory. (**D**) Schematic representation of the frontier molecular orbitals of $C_2H_4^+$ in its D_0 and D_1 electronic states.

8

character switched from D_1 to D_0 without change of the molecular structure. This sudden shift, confirmed by the experimental observations, is explained by the difference in the 1s$\to \pi^*$ transition energies from the D_0 and D_1 states (Fig. 2**E**). This large splitting is the consequence of electron correlation, i.e. it results from the different occupations of the two orbitals lying below the π^* orbital (see Fig. 3**D**). This direct spectroscopic mapping of electronic-state switching at a CI can be expected to be a general feature of ATAS. A similar effect was also observed in the case of the 1s$\to \pi$ transition (lines centered at 281 eV), but its contribution to the dynamic (and experimental) D_1 spectra is suppressed by the axis distribution created by strong-field ionization (Section S4).

This sudden shift of the 1s$\to \pi^*$ transition energy with the change in electronic character is indeed key to unambiguously observing the ultrafast $D_1 \to D_0$ relaxation. Figure 2**D** shows the populations of the adiabatic D_1 and D_0 states as a function of the delay following preparation of the D_1 state. The D_1 population decays by 70 % at the first encounter with the CI, which begins to occur within 5 fs. The combination of this short time with the highly efficient population transfer explains the observed electronic-relaxation time scale of 6.8$\pm$0.2 fs. The slower time constant of the bi-exponential decay is caused by residual population in the D_1 state that decays at later returns of the excited-state wave packet to the CI, causing the later steps in the population curves.

In addition to the non-adiabatically evolving wave packet in the D_1 state, the pump pulse also prepared a wave packet in the D_0 state that evolved adiabatically with respect to its electronic character. This fact is most clearly visible through the periodic oscillation of the absorption band centered at 281 eV in Figs. 1**D** and 1**E**. The contribution of the D_0 wave packet to the observed dynamics is further detailed in Fig. 3**A**. The transient spectra are dominated by the 1s$\to \pi$ and 1s$\to \pi^*$ bands that display opposite energy shifts as a function of delay. This observation is explained by static X-ray spectra (Fig. 3**C**) calculated at the FC point and the equilibrium geometry of the D_0 state. These spectra confirm the opposite energy shifts of the two absorption bands caused by the structural-relaxation dynamics in the D_0 state. The spectral intensities of the 1s$\to \pi^*$ band in measurements and calcula-

9

tions are compared in Fig. 3**B**. Here, the contributions of both the D_1 and the D_0 states to the 1s$\rightarrow \pi^*$ band were included because of their spectral overlap in the calculations. A bi-exponential fit to these data again yielded short time constants of 6.2$\pm$0.3 fs (experiment) and 10.7$\pm$0.1 fs (theory), which were dominated by the $D_1 \rightarrow D_0$ electronic relaxation.

These results suggest that X-ray absorption spectroscopy might also be directly sensitive to structural dynamics, in addition to the electronic dynamics discussed above. A Fourier transform of the center position of the 1s$\rightarrow \pi$ and 1s$\rightarrow \pi^*$ bands (Figs. 4**A,C**) indeed revealed two dominant frequencies (37.7$\pm$3.3 and 13.5$\pm$3.3 THz). These values were assigned to the fundamental CH_2 scissor mode ($v_3 = 1$) and the overtone of the CH_2 torsion ($v_4 = 2$), respectively. The analysis of calculations performed over longer delays suggested the population of a third vibrational mode, the symmetric C=C stretch vibration, with a frequency of 45 THz (Section S2.6), which explained the high-frequency shoulder observed in the experimental data in Fig. 4**C**. The dominant population of these three vibrational modes reflected the change in equilibrium geometry from the electronic ground state of ethylene to that of its cation. Whereas neutral ethylene is planar, its cation has a twisted equilibrium geometry with an angle of $\sim$29.2° between the two planes defined by the CH_2 units (*24, 42*), a stretched CC bond length and an increased HCH angle (Fig. S7). Our dynamical simulations showed that vertical ionization of S_0 to D_0 resulted in significant excitation of all three vibrational modes (Fig. S10). These three vibrational frequencies were indeed also observed in the Fourier transform of the measured line positions, which illustrated the direct mapping of structural dynamics into SXR-ATAS spectra. We note that it is not the fundamental of the torsional frequency that was excited, but its overtone, because the former has A_u symmetry in the $D_{2h}(M)$ symmetry group and thus a vanishing Franck-Condon factor, whereas the latter is totally symmetric.

The direct mapping of structural dynamics into the spectral position of X-ray absorption lines is a useful property for tracing ultrafast structural dynamics with element sensitivity. In the present case, this sensitivity originates from a strong variation of the energy of the 1s$\rightarrow \pi$ and 1s$\rightarrow \pi^*$ transitions
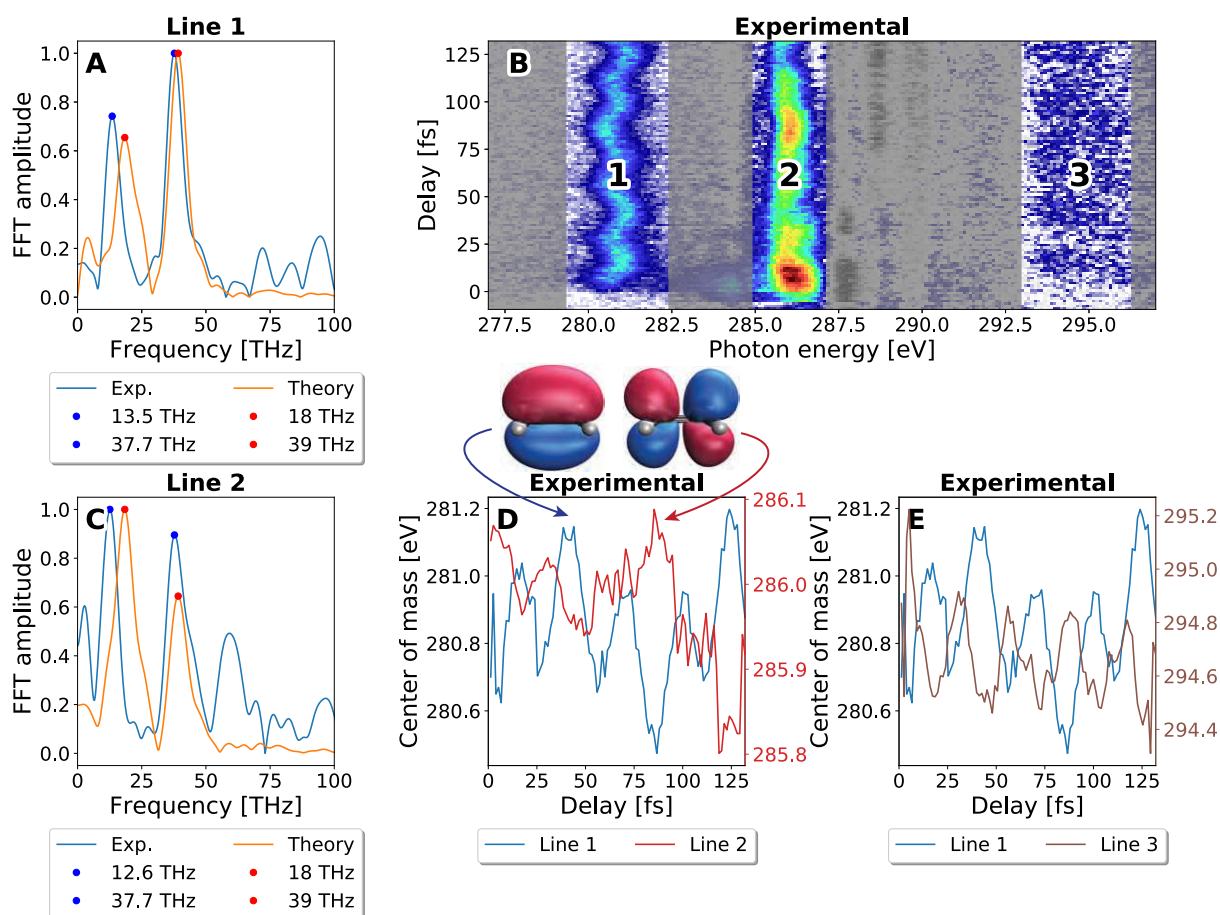
Figure 4: **Electronic-structure encoding in vibrational dynamics probed by ATAS**. Fourier transforms of the center of mass of the absorption bands "1" centered at 281 eV (**A**) and "2" centered at 286 eV (**C**). (**B**) Overview of the transient-absorption spectra. (**D**) Time-dependent shifts in the center positions of bands "1" and "2", assigned in terms of the (particle) natural transition orbitals dominating the corresponding positions. (**E**) Same as (**D**) for the center positions of bands "1" and "3".

with the excited vibrational modes (see Figs. S18, S19). The mapping of structural dynamics to X-ray absorption line positions thus simultaneously provides information on the electronic character of the states involved in the X-ray transition.

This electronic-structure encoding is further illustrated by the fact that the central positions of the 1s→ π and 1s→ π^* bands modulated out of phase, both in the experimental (Fig. 4**B**) and the theoretical data (Fig. 3**A**). These observations were related to the electronic-structure properties through the calculated (particle) natural transition orbitals (NTOs), shown in Fig. 4**D**. Whereas the NTO for the 1s→ π band has bonding character without nodal planes perpendicular to the C=C bond, the NTO for the 1s→ π^* band has anti-bonding character and one nodal plane perpendicular to the C=C axis. The out-of-phase modulation observed in the experiment hence directly reflects the different electronic properties of the final states of the core-level excitation. Interestingly, this property is not limited to the two discussed bands. Figure 4**E** shows that the central position of the band 3, centered at 295 eV, also modulates out of phase with the 1s→ π band. Highly accurate calculations in this spectral domain remain challenging because transitions to both (high) Rydberg states and the continuum may contribute. The experimental results however suggested that the electronic-structure encoding demonstrated for the lower-lying transitions also extends to the Rydberg/continuum part of the spectrum, which offers interesting perspectives for time-resolved near- and extended-edge X-ray absorption fine-structure (NEXAFS/EXAFS) studies.

We have demonstrated attosecond transient-absorption spectroscopy at the carbon K-edge and have used it to reveal the fastest electronic relaxation process in molecular systems measured to date. We have shown that the technique is particularly powerful in revealing electronic-state switching at conical intersections, a property that we have traced back to electron correlation. Moreover, the technique simultaneously displayed a pronounced sensitivity to multi-dimensional structural dynamics, including electronic-structure encoding. This study showed that electronic relaxation can take place on time scales below the shortest vibrational periods. This finding supports the feasibility of elec-

tronic coherent control over conical-intersection dynamics (*43*) because electronic coherence might be sufficiently long-lived (*44*). It further revealed the crucial importance of sub-femtosecond spectroscopies for fully understanding excited-state dynamics in molecules through a clean separation of electronic and structural dynamics. The extension of ATAS from the XUV domain to the carbon K-edge generalizes the considerable potential of this method to the broad class of organic molecules and thereby opens a wide range of opportunities, such as access to the ultimate time scale of the retinal isomerization reaction (*45, 46*). It will also enable studies of solvated molecules (*47*) that can now be extended from the femtosecond (*48*) to the attosecond time scale, giving access to the effects of solvation on the time scales of CI dynamics and electronic decoherence.

Acknowledgments

Supplementary materials

Materials and Methods

Supplementary Text

Figs. S1 to S20

Tables S1-S2

References (*50–56*)

References and Notes

1. W. Domcke, D. R. Yarkony, H. Köppel, eds., *Conical intersections: Electronic structure, dynamics and spectroscopy*, vol. 15 of *Adv. Ser. in Phys. Chem.* (World Scientific, Singapore, 2004).

2. M. S. Schuurman, A. Stolow, *Annual review of physical chemistry* **69**, 427 (2018).

3. A. L. Sobolewski, W. Domcke, C. Hättig, *Proceedings of the National Academy of Sciences* **102**, 17903 (2005).

4. R. Schoenlein, L. Peteanu, R. Mathies, C. Shank, *Science* **254**, 412 (1991).

5. D. Polli, *et al.*, *Nature* **467**, 440 (2010).

6. S. M. Falke, *et al.*, *Science* **344**, 1001 (2014).

7. G. Sansone, *et al.*, *Nature* **465**, 763 (2010).

8. P. M. Kraus, *et al.*, *Science* **350**, 790 (2015).

9. F. Calegari, *et al.*, *Science* **346**, 336 (2014).

10. M. Huppert, I. Jordan, D. Baykusheva, A. von Conta, H. J. Wörner, *Phys. Rev. Lett.* **117** (2016).

11. J. Vos, *et al.*, *Science* **360**, 1326 (2018).

12. S. Biswas, *et al.*, *Nat. Phys.* **16**, 778 (2020).

13. V. Loriot, *et al.*, *Journal of Physics: Photonics* **2**, 024003 (2020).

14. I. Jordan, *et al.*, *Science* **369**, 974 (2020).

15. E. Goulielmakis, *et al.*, *Nature* **466**, 739 (2010).

16. A. Wirth, *et al.*, *Science* **334**, 195 (2011).

17. C. Ott, *et al.*, *Nature* **516**, 374 (2014).

18. S. M. Teichmann, F. Silva, S. L. Cousin, M. Hemmer, J. Biegert, *Nature Communications* **7**, 11493 (2016).

19. A. Johnson, *et al.*, *Structural Dynamics* **3**, 062603 (2016).

20. Y. Kobayashi, K. F. Chang, T. Zeng, D. M. Neumark, S. R. Leone, *Science* **365**, 79 (2019).

21. N. Saito, *et al.*, *Optica* **6**, 1542 (2019).

22. H. J. Wörner, *et al.*, *Science* **334**, 208 (2011).

23. H. Timmers, *et al.*, *Nature communications* **10**, 1 (2019).

24. H. Kppel, W. Domcke, L. S. Cederbaum, W. v. Niessen, *The Journal of Chemical Physics* **69**, 4252 (1978).

25. C. Sannen, G. Raşeev, C. Galloy, G. Fauville, J. Lorquet, *The Journal of Chemical Physics* **74**, 2402 (1981).

26. M. Ben-Nun, T. J. Martınez, *Chemical physics letters* **298**, 57 (1998).

27. J. Quenneville, T. J. Martinez, *The Journal of Physical Chemistry A* **107**, 829 (2003).

28. T. J. Martinez, *Accounts of chemical research* **39**, 119 (2006).

29. K. Kosma, S. A. Trushin, W. Fuß, W. E. Schmid, *The Journal of Physical Chemistry A* **112**, 7514 (2008).

30. H. Tao, *et al.*, *The Journal of chemical physics* **134**, 244306 (2011).

31. T. Allison, *et al.*, *The Journal of chemical physics* **136**, 124317 (2012).

32. T. Kobayashi, T. Horio, T. Suzuki, *The Journal of Physical Chemistry A* **119**, 9518 (2015).

33. S. Pabst, M. Lein, H. J. Wörner, *Phys. Rev. A* **93**, 023412 (2016).

34. M. Ben-Nun, T. J. Martnez, *Ab Initio Quantum Molecular Dynamics* (John Wiley & Sons, Ltd, 2002), pp. 439–512.

35. S. P. Neville, *et al.*, *Faraday discussions* **194**, 117 (2016).

36. S. P. Neville, M. Chergui, A. Stolow, M. S. Schuurman, *Physical review letters* **120**, 243001 (2018).

37. I. Seidu, *et al.*, *The Journal of Chemical Physics* **151**, 144104 (2019).

38. Y. Pertot, *et al.*, *Science* **355**, 264 (2017).

39. A. R. Attar, *et al.*, *Science* **356**, 54 (2017).

40. B. Joalland, T. Mori, T. J. Martnez, A. G. Suits, *The Journal of Physical Chemistry Letters* **5**, 1467 (2014). PMID: 26269995.

41. A. Ludwig, *et al.*, *The Journal of Physical Chemistry Letters* **7**, 1901 (2016). PMID: 27139223.

42. S. Willitsch, U. Hollenstein, F. Merkt, *The Journal of Chemical Physics* **120**, 1761 (2004).

43. M. F. Kling, P. von den Hoff, I. Znakovskaya, R. de Vivie-Riedle, *Phys. Chem. Chem. Phys.* **15**, 9448 (2013).

44. M. Vacher, M. J. Bearpark, M. A. Robb, J. P. Malhado, *Physical Review Letters* **118**, 083001 (2017).

45. P. J. Johnson, *et al.*, *Nature chemistry* **7**, 980 (2015).

46. R. A. Mathies, *Nature chemistry* **7**, 945 (2015).

47. C. Kleine, *et al.*, *The journal of physical chemistry letters* **10**, 52 (2018).

48. A. D. Smith, *et al.*, *The journal of physical chemistry letters* **11**, 1981 (2020).

49. K. S. Zinchenko, *et al.*, *Zenodo* (2020). https://doi.org/10.5281/zenodo.4293679.

50. R. McLaren, S. A. C. Clark, I. Ishii, A. P. Hitchcock, *Phys. Rev. A* **36**, 1683 (1987).

51. A. Hitchcock, C. Brion, *Journal of Electron Spectroscopy and Related Phenomena* **18**, 1 (1980).

52. R. Santra, L. S. Cederbaum, *The Journal of Chemical Physics* **115**, 6853 (2001).

53. K. Kaufmann, W. Baumeister, M. Jungen, *Journal of Physics B: Atomic, Molecular and Optical Physics* **22**, 2223 (1989).

54. T. J. Park, J. C. Light, *The Journal of Chemical Physics* **85**, 5870 (1986).

55. V. Lebedev, *USSR Computational Mathematics and Mathematical Physics* **15**, 44 (1975).

56. V. Lebedev, *USSR Computational Mathematics and Mathematical Physics* **16**, 10 (1976).

Supplementary Material for:
Sub-7-femtosecond conical-intersection dynamics probed at the carbon K-edge

Kristina S. Zinchenko[1,*], Fernando Ardana-Lamas[1,*,†], Issaka Seidu[2,*],
Simon P. Neville[2,*], Joscelyn van der Veen[2,*], Valentina Utrio Lanfaloni[1],
Michael S. Schuurman[2,‡], Hans Jakob Wörner[1,‡]

[1] Laboratorium für Physikalische Chemie, ETH Zürich, 8093 Zürich, Switzerland
[2] National Research Council of Canada, Ottawa, Canada
* These authors contributed equally to this work
† Present Address: European XFEL GmbH, Schenefeld, Germany
‡ **E-mails: michael.schuurman@nrc-cnrc.gc.ca, hwoerner@ethz.ch**

Materials and Methods

Supplementary Text

Figs. S1 to S20

Tables S1 and S2

References *(50-56)*

S1 Experimental setup

A schematic diagram of the experimental setup is shown in Figure 1**A** of the main text. The laser system consists of a regenerative and a cryogenically-cooled amplifier (Coherent) delivering 19 mJ, 28 fs pulses, centered at 800 nm at 1 kHz repetition rate. These pulses are used to pump a BBO-based parametric amplifier (HE-TOPAS, Light Conversion), generating mid-infrared (mid-IR) pulses with an average pulse energy of 2.5 mJ centered at 1.8 μm (idler). This mid-IR output is then compressed down to less than two optical cycles 10.4$\pm$1.5 fs (average of three measurements) in an argon-filled hollow-core fiber with about 72% throughput, followed by compression in bulk glass. The temporal and spectral profiles of the compressed sub-two cycles pulses were measured with a Wizzler device (Fastlite) and are shown in Figure S1.
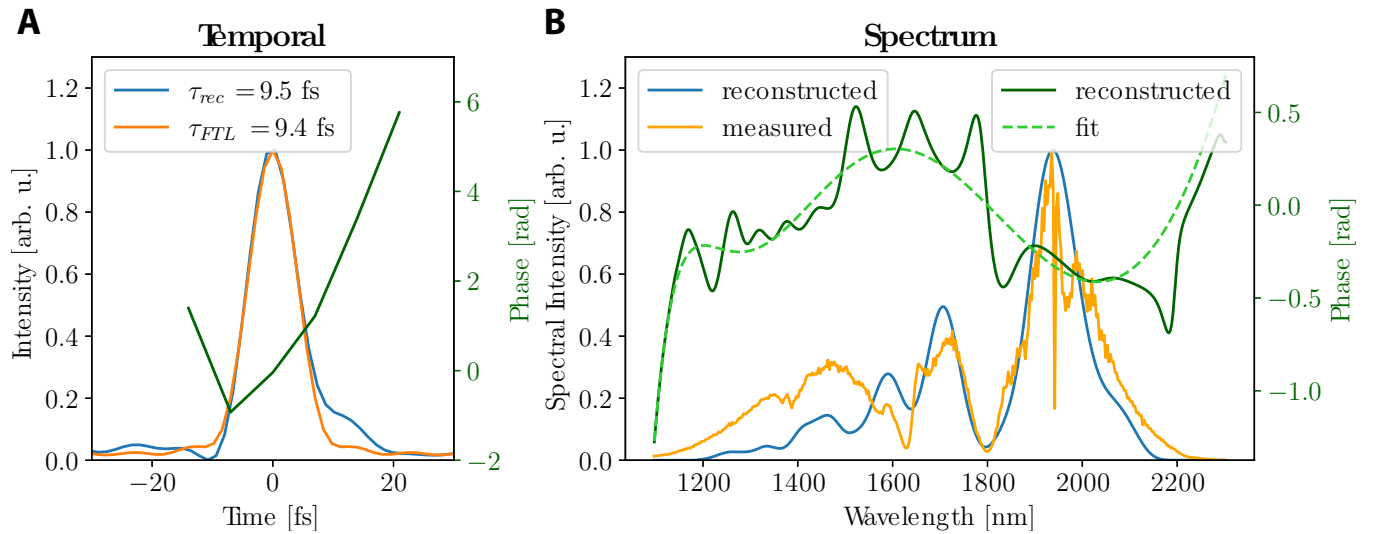

Figure S1: **Output of the hollow-core fiber for an 1800-nm-input pulse.** (**A**) Single-shot reconstructed temporal profile of the compressed mid-IR pulses yielding a 9.5 fs FWHM pulse (blue curve) and its temporal phase (green curve). The Fourier limit is 9.4 fs FWHM (orange curve). The pulse duration quoted in the (main) text is an average of three measurements and is equal to 10.4$\pm$1.5 fs. (**B**) Normalized spectral amplitudes of the measured (orange line) and of the reconstructed (blue line) spectra of the compressed pulse. The green solid and dashed lines correspond to the retrieved and fitted spectral phase of the pulse, respectively.

The hollow-core fiber output is then split in pump and probe beams by a partially reflective mirror (R70:T30), hereinafter referred to as a beam splitter (BS). It covers the wavelength range between 1 and 2.2 μm, sufficient for our mid-IR pulse. The pump beam, transmitted through the BS, is used to excite the sample, whereas the probe beam, reflected from the BS, is used to generate a soft-X-ray (SXR) continuum in order to probe the dynamics induced by the pump pulse. The probe beam is focused by a silver off-axis parabolic mirror with a focal length of 250 mm into a helium-filled gas target for high-order harmonic generation (HHG). The generated SXR beam is then transmitted through a set of three pinholes to remove the driving mid-IR beam. A small residual fraction of the driving mid-IR pulse does not influence the dynamics discussed in the paper, and, therefore, is not filtered by a metallic filter allowing for a shorter data-acquisition time. Afterwards, the SXR beam is incident on a toroidal mirror such that the generation focus is imaged in a $2f$-to-$2f$-configuration, resulting in a total separation between the two foci of 1.2 m. Thus, the SXR focus in the interaction chamber is estimated to be a 1:1 image of the focus in the generation region.

The pump beam is directed on a mirror pair fixed on top of a translation stage for varying the time delay during pump-probe measurements. After the delay line, the mid-IR beam is guided towards the rectangular recombination chamber, where it is focused with a parabolic mirror (f=400 mm) onto the target sample, leading to a focal spot size of approximately 70 μm. Since the pump beam is reflected from the perforated recombination mirror, only 0.4 mJ reach the sample. A mechanical shutter is implemented into the pump path to perform "pump on - pump off" measurements at each delay step. Reference spectra without sample gas were additionally recorded before and after each full scan.

Both, the mid-IR pump and the SXR probe beams are recombined with a perforated prism-shaped silver mirror and propagate co-linearly towards the sample target. After the interaction region, the mid-IR beam is filtered by a thin aluminum filter, whereas the SXR beam is imaged

3

by an aberration-corrected flat-field grating (2400 lines/mm) on a vacuum CCD camera. A slit at the entrance to the spectrometer is used only as an alignment tool.

S2 Data analysis

S2.1 Static spectra

Figure S2 shows the SXR continuum generated in helium spanning up to 450 eV (blue line) and the spectrum after transmission through the C_2H_4 gas (orange). The SXR absorption of neutral C_2H_4 in its electronic ground state (S_0) is dominated by the transition from the carbon $1s$ shell to the unoccupied orbital of dominant π^* character with a peak at 284.8 eV, followed by the onset of a broad continuum absorption.
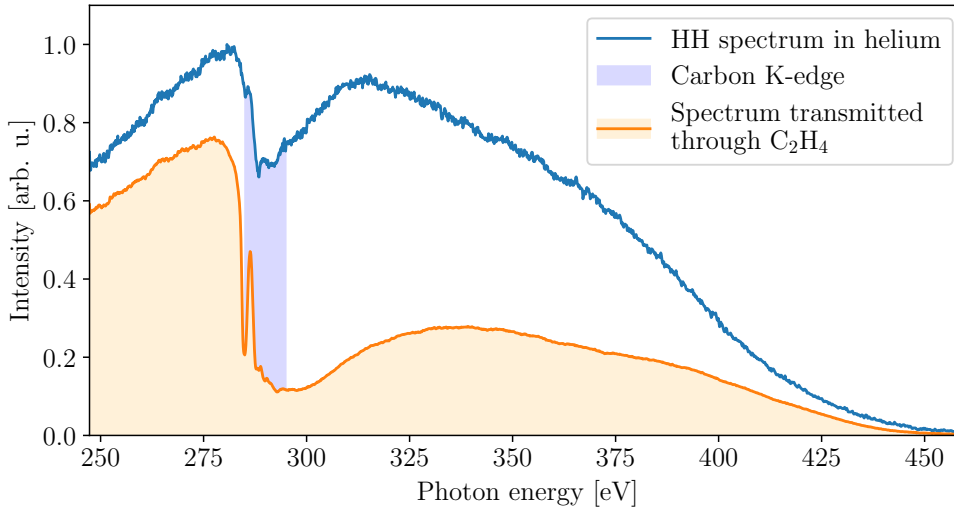

Figure S2: **High-harmonic spectrum generated in helium (blue) and the spectrum transmitted through C_2H_4 gas (orange).** The local minimum in the blue spectrum originates from carbon contamination on the optical components. The additional absorption (blue-shaded area) originates from carbon K-edge absorption of C_2H_4.

The optical density $OD(\hbar\omega)$, shown in Figure **1B** (red line) of the main text, is defined as:

$$OD(\hbar\omega) = \log_{10} \frac{I_0(\hbar\omega)}{I_{pump\ off}(\hbar\omega)}, \tag{1}$$

4

Table S1: Assignment of the carbon K-edge SXR absorption spectrum of the C_2H_4 (D_{2h}) molecule. Data is taken from (*50*).

Feature	Edge	Energy[eV]	Assignment
1	C K	284.7	$1s \rightarrow \pi^*$
2	C K	287.4	$1s \rightarrow 3s$
3	C K	287.8	$1s \rightarrow 3p$
4	C K	289.3	$1s \rightarrow 4p$

where $I_0(\hbar\omega)$ is the reference spectral intensity, i.e., the spectrum recorded without sample, and $I_{pump\ off}(\hbar\omega)$ is the spectrum after transmission through the sample, i.e., the spectrum of the non-ionized sample. Both $I_0(\hbar\omega)$ and $I_{pump\ off}(\hbar\omega)$ are background-corrected.

The spectral calibration of the image, acquired with our spectrometer, is based on the absorption bands of ethylene at the carbon K-edge (284.8, 286.4, and 287.9 eV (*50*), and 285.0, 288.5, and 292.0 eV due to the carbon contamination of the SXR reflective optics) and the nitrogen K-edge of N_2 (at 400.0 eV (*51*)) as a reference at higher photon energy. As a cross-check of the performed calibration, argon $L_{2,3}$ absorption lines have been used.

S2.2 Change in optical density

The change over time in optical density $\Delta OD(\hbar\omega, \tau_d)$ can be calculated relative to the spectrum of an unpumped sample, $I_{pump\ off}(\hbar\omega)$, and the time-dependent spectrum of the pumped sample, $I_{pump\ on}(\hbar\omega, \tau_d)$. Thus, the $\Delta OD(\hbar\omega, \tau_d)$, shown in Figure **1D** of the main text, as follows:

$$\Delta OD(\hbar\omega, \tau_d) = \log_{10} \frac{I_{pump\ off}(\hbar\omega)}{I_{pump\ on}(\hbar\omega, \tau_d)}, \tag{2}$$

At each time delay, the pumped and unpumped absorption spectra are averaged over 50 images, integrated over 0.5 s each. The theoretical $\Delta OD(\hbar\omega, \tau_d)$ spectra have been linearly shifted up by 3.25 eV to match the experimental $\Delta OD(\hbar\omega, \tau_d)$ spectra.

S2.3 Background correction

Since in the present work, we have focused on the dynamics at the carbon K-edge, only a pre-edge background correction is applied to the experimental S_0 spectrum (Figure S3A). It is performed by subtracting an error-function fitting from the optical-density curve, calculated according to Eq. (1). The experimental $\Delta OD(\hbar\omega, \tau_d)$ is background-corrected by subtracting an average of the 271-276 eV region at each time step.

S2.4 X-ray absorption spectra of ethylene and its cation

Figure S3 shows an overview of the spectral data, their assignment and comparison with the calculated spectra, which are further described in Section S3.

S2.5 Zero time delay and decay fitting

The determination of the zero time delay has been done with the following method. The experimental D_1 line of ΔOD is integrated between E_1=283.4 and E_2=285.0 eV. The resulting $\int_{E_1}^{E_2} \Delta OD_T(\hbar\omega, \tau_d)d\hbar\omega = I(\tau_d)$ is used to fit the following pulse function:

$$
\begin{aligned}
I_{bi\ fit}(t) &= \Phi(t - t_0) * D(t - t_0, t_{d_1}, t_{d_2}) + b \\
&= \frac{1}{2}\left[1 + \mathrm{erf}\left(\frac{t - t_0}{\sqrt{2}\sigma}\right)\right] * \left[a_1\ \exp\left(-\frac{t - t_0}{t_{d_1}}\right) + a_2\ \exp\left(-\frac{t - t_0}{t_{d_2}}\right)\right] + b,
\end{aligned}
\tag{3}
$$

which is a product of a cumulative-distribution function Φ and a bi-exponential decay function D. Parameters of the Gauss error function erf are t_0 and σ and correspond to the position of the center and the root-mean-square width of the Gaussian, respectively. The time constant τ_G, equivalent to the full width at half maximum (FWHM) of the Gaussian, is calculated as follows:

$$
\tau_G = 2\sqrt{2\ln 2}\sigma. \tag{4}
$$

$t_{d_{1,2}}$ are decay constants with $a_{1,2}$ amplitudes, and the b constant is the vertical offset.

6

When fitting Eq. (3) to the experimental and theoretical D_1 lines, all variables are treated as fitting parameters, but τ_G is fixed to 10.5 fs and 10.0 fs for the experimental and calculated data sets, respectively. The theoretical constant $\tau_G = 10.0$ fs corresponds to the FWHM of the Gaussian function used to convolve the calculated data for comparison with the experimental data. The mean values of the parameters and standard deviations are determined from at least
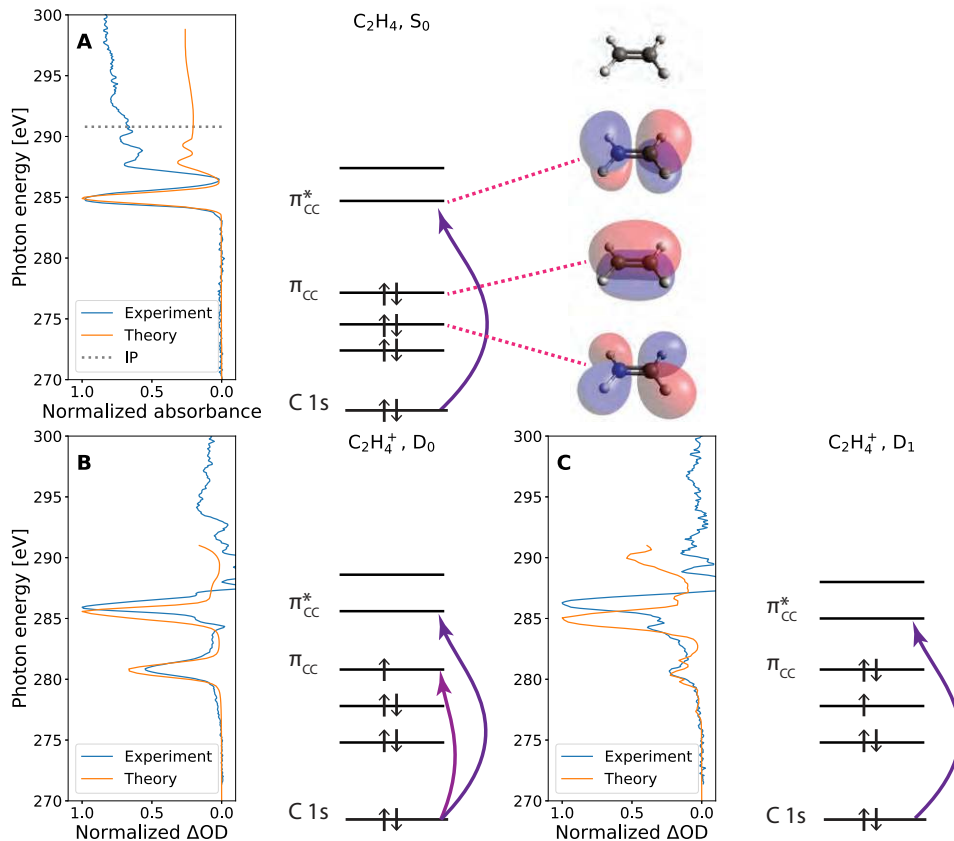

Figure S3: **X-ray absorption spectra of ethylene and its cation** (**A**) Static X-ray-absorption spectrum of C_2H_4 in its electronic ground state (S_0) and illustration of the most relevant molecular orbitals. (**B**) X-ray absorption spectrum of $C_2H_4^+$ in its electronic ground state (D_0), obtained by integrating transient X-ray spectra over pump-probe delays greater than 21.3 fs in experimental, and greater than 21.6 fs in calculated data. (**C**) Transient X-ray absorption spectrum of the D_1 state of $C_2H_4^+$, obtained by integrating over pump-probe delays of -9.4 and 10.6 fs in experimental, and of -9.6 and 21.6 fs in calculated data. All panels show experimental data (blue) compared to calculated (DFT/MRCI) spectra (orange).
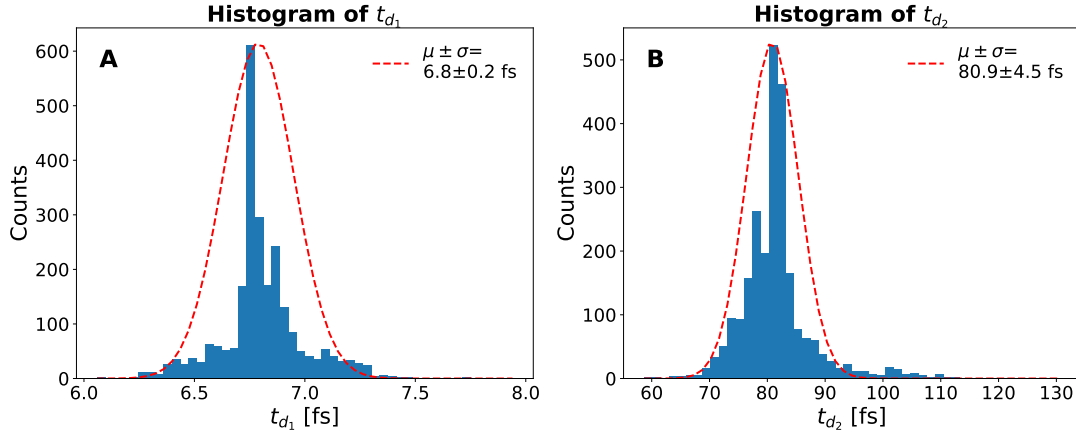
Figure S4: **Statistics of fitting Eq. 3 to the experimental D_1 line (Fig. 2B)**. A,B) Histograms and distribution functions of the obtained fit results using 2500 independent fitting runs with independent initial guesses.
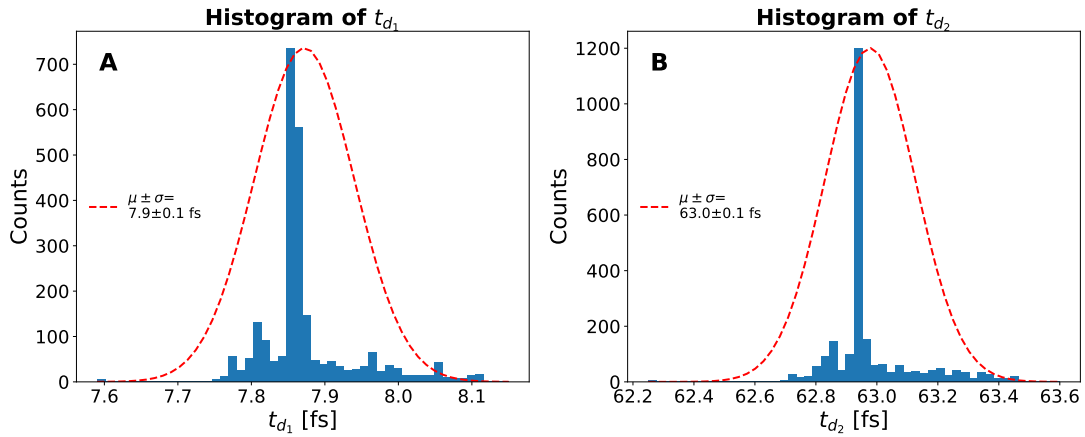

Figure S5: **Same as Fig. S4 for the theoretical D_1 line (Fig. 2B)**.

2500 independent runs of the fitting algorithm with randomly chosen initial guesses (Figs. S4 and S5). The fitting procedure includes relaxed boundary conditions. The correspondence between the symbols used here and in the main text is $t_{d_1} \leftrightarrow \tau_1$ and $t_{d_2} \leftrightarrow \tau_2$.

The determination of decay constants for the absorption bands centered at 284-286 eV (Figures 2**B** and 3**B**) has been done with the above-mentioned method as well. The complete set of fit parameters and standard deviations are given in Table S2.

Table S2: Fitting parameters for the results shown in Figures 2**B** and 3**B**

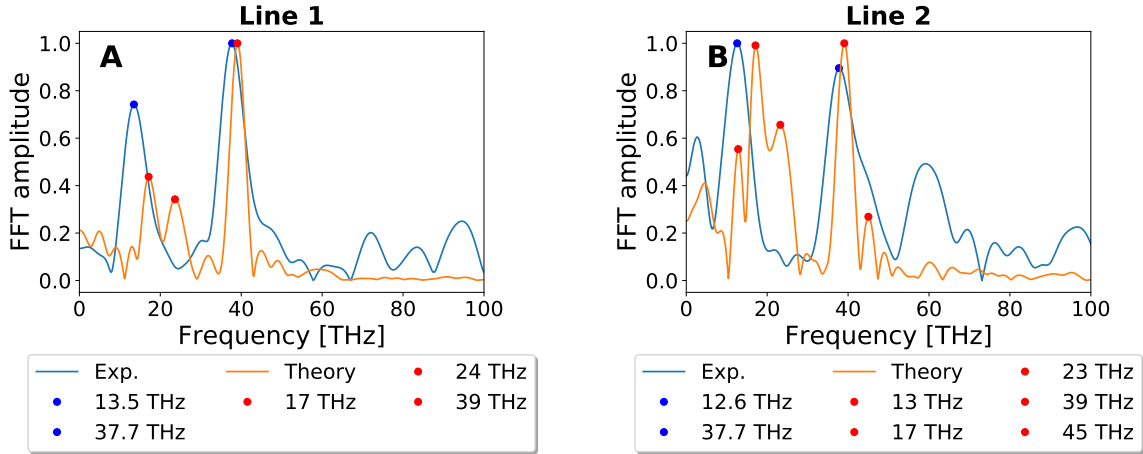|	t_0 [fs]	$t_{0,std}$	t_1 [fs]	t_{d_1} [fs]	$t_{d_1,std}$ [fs]	t_{d_2} [fs]	$t_{d_2,std}$ [fs]	$\tilde{\chi}^2$
Line 1 (D_1)								
Experiment	0.0	0.14	10.5	6.8	0.2	80.9	4.5	0.0055
Theory	0.0	0.03	10.0	7.9	0.1	63.0	0.1	0.0176
Line 2 (D_0)								
Experiment	1.61	0.26	10.5	6.2	0.3	140.0	2.4	0.0891
Theory	0.12	0.03	10.0	10.7	0.1	501.9	3.5	0.0220

S2.6 Vibrational analysis

Figure S6: **Fourier transforms of the center-of-mass of the absorption bands "1" centered at 281 eV (A) and "2" centered at 286 eV (B)**. The FFT of the experimental (theoretical) data sets are taken over their entire lengths, which amounts to 300 fs (488.8 fs).

For the vibrational analysis, each absorption line of interest has been isolated from the experimental and theoretical $\Delta OD(\hbar\omega, \tau_d)$ data sets. Next, the center of mass of the isolated line is calculated for every spectrum at each time step. The obtained center of mass as a function of time delay is then Fourier-transformed (with Hanning window and zero-padding ten times the length of the dataset). The FFT of the experimental data was taken for better accuracy from a dataset registered over 300 fs on the same day as the data in Figure 1**D**. The FFT of the experimental data results in two dominant frequencies at 13±3.3 THz and 38±3.3 THz,

corresponding to the fundamental C-H in-plane bending ($\nu_3 = 1$) and the overtone of the CH_2 torsion ($\nu_4 = 2$), respectively. The FFT of the theoretical data, taken over the same delay range as in the experiment (about 300 fs, shown in Fig. 4**A,C**), results in the same dominant frequencies (18 THz and 39 THz). The FFT of the theoretical data, taken over the complete calculated data set spanning over almost 500 fs (between 8.60 and 497.40 fs), is shown in Figure S6. It results in dominant frequencies at 17 THz and 39 THz, which agree with the experimental data within the expected accuracy of the calculations. In Figure S6**B**, an additional peak is observed at a frequency of 45 THz, which is assigned to the symmetric C=C stretching vibration. Hence, the high-frequency shoulder of the 38 THz peak observed in the experimental data might also be assigned to the fundamental C=C stretching. The literature values of the aforementioned vibrations are 13.14 THz, 37.73 THz, and 44.60 THz, corresponding to the overtone of the CH_2 torsion, the fundamental C-H in-plane bending, and the C=C stretching, respectively (*42*).

S3 Ab-initio multiple spawning and X-ray absorption calculations of $C_2H_4^+$

S3.1 Non-adiabatic Dynamics

The ultrafast electronic relaxation of the initially prepared D_1 state of $C_2H_4^+$ proceeds via planar conical intersections located near the Franck-Condon region. Indeed, as previous work has shown (*40, 41*), while this planar moiety is not the global-minimum-energy D_0/D_1 conical intersection, it is the region of the conical intersection seam that is exclusively accessed when population is placed on the D_1 electronic state at nuclear structures in the vicinity of the S_0 minimum. As Figure S7 evinces, the D_0/D_1 intersection is accessed via contraction of the C=C bond (1.337 Å to 1.251 Å) and scissoring of the CH_2 bond angle ($117.1°$ to $94.1°$).

Furthermore, as Figure S8 shows, the path to the MECI is energetically barrierless. The relatively small displacements from the Franck-Condon region, coupled with gradient directed
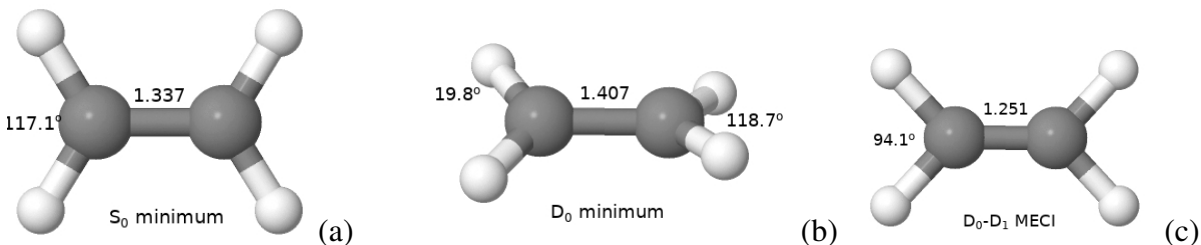
10

Figure S7: Optimized structures for the (a) ground electronic state of neutral C_2H_4, (b) the ground electronic state of $C_2H_4^+$ at the cc-pVTZ/CCSD(T) level of theory, and the (c) planar minimum-energy D_0/D_1 conical intersection at the 3s2p1d(ANO)/MR-CIS level of theory.

nuclear motion to the coupling region, results in ultrafast relaxation to the D_0 state following ionization to the D_1 state.
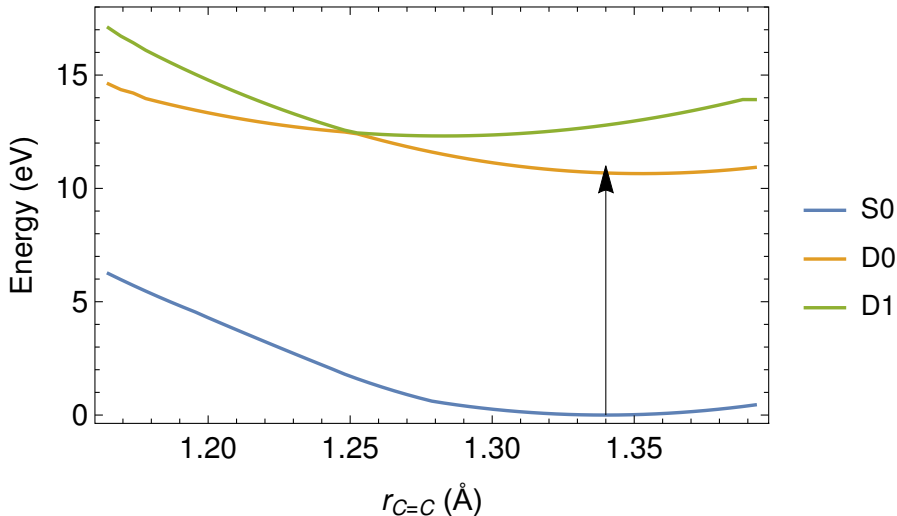

Figure S8: Potential energy curves for S_0, D_0, and D_1 states along the C=C stretch coordinate at the MR-CIS/cc-pVTZ level of theory. The black arrow indicates the vertical ionization potential(s).

This prompt decay is observed in the *ab initio* multiple spawning (AIMS) simulations employed to describe the coupled electronic-nuclear dynamics in the lowest two electronic states of the cation. Trajectories were initialized either on the ground D_0 or first excited D_1 state in separate dynamical simulations. To generate initial conditions, the phase-space density corre-
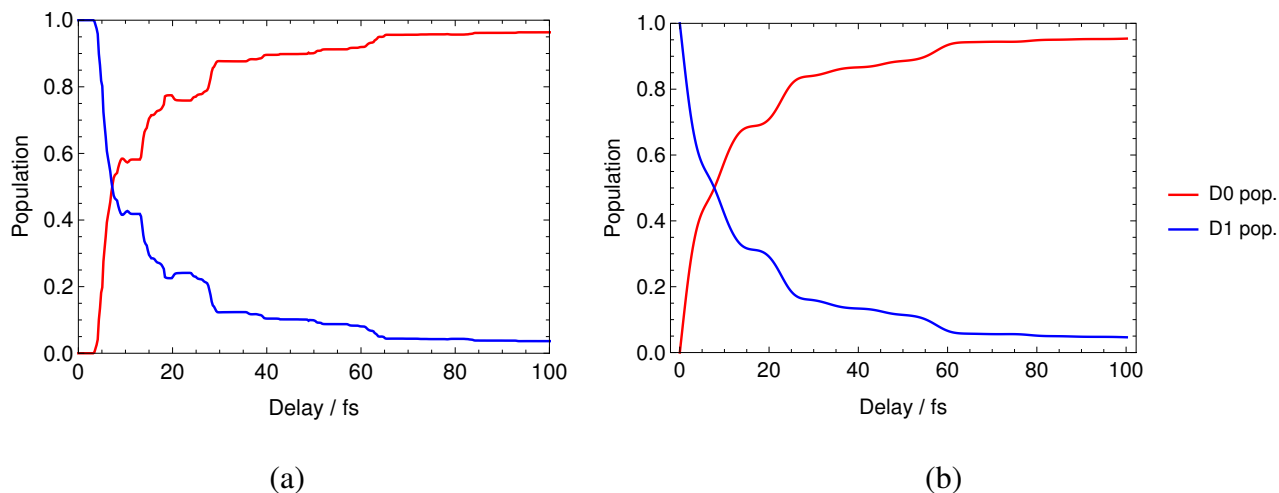
11

Figure S9: Adiabatic state populations from AIMS simulation in which 24 trajectory basis functions were initialized on the D_1 electronic state. Shown here are the nascent adiabatic populations (a), and the populations curves convoluted with a Gaussian function with FWHM=5 fs (b).

sponding to the ground vibrational state of the neutral molecule was sampled to generate points at which to initialize the trajectory basis functions on the D_0 and D_1 electronic states. Thus, the simulation implicitly assumes that the initial neutral molecules were in the ground vibrational state and that ionization vertically "lifts" the initial state wavefunction onto the cationic manifold. For both simulations, 24 initial conditions were employed (yielding 48 initial trajectory basis functions in total). For trajectory basis functions initialized on the ground cationic state, purely vibrational dynamics resulted, i.e. no spawning to D_1 was observed). However, the simulation in which trajectory basis functions were initialized on D_1 resulted in extremely rapid spawning down to the D_0 state. Figure S9 shows that the D_1 electronic population is rapidly "dumped" to the D_0 state in <10 fs. Analysis of the trajectory results leads to an assignment of the rapid initial decay to the first passage through the CI region. Subsequent passes through this region are visible as discrete "steps" in nascent population curves in Fig. S9(a). The effect of convolution by a Gaussian function with a FWHM of 5 fs, as used in comparing experimental and theoretical XAS spectra is illustrated in Fig. S9(b).

To elucidate the specific vibrational motions that characterize the evolution of the nuclear wave packet, the AIMS wave-function densities (which are propagated in an atom-centered Cartesian coordinate basis) were numerically integrated to yield reduced nuclear densities with respect to valence internal coordinates. The D_0 nuclear reduced densities along the C=C stretch, symmetric CH_2 scissoring (or C-H in-plane bending) coordinate, and dihedral angle about the C=C bond were obtained via Monte-Carlo integration and are plotted in Figure S10. These three coordinates represent the largest-amplitude vibrational displacements of the wave packet prepared through ionization.

Conversely, significant electronic relaxation from D_1 is observed in less than a single vibrational period along the C=C stretch. As Figure S10 shows, the majority of the D_1 population is depleted upon the wave packet reaching the classical turning point of the C=C stretch vibration. Indeed, the adiabatic population curves, shown in Figure S9, show a near total transfer of excited-state population to the ground electronic state within <10 fs, in excellent agreement with the timescale measured experimentally.

Interestingly, there is significant torsional motion on the D_0 state, as shown by Figure S10(e). Since the minimum-energy structure of the cationic ground state displays a significant twisting angle of 29.2°, ionization from planar S_0 structures results in significant excitation of the torsional mode (*24, 42*). However, as Figure S17 shows, this motion does not result in appreciable shifts of the peaks in the XAS spectrum. Accordingly, this motion is not effectively imaged by TRXAS.

S3.2 X-ray Absorption Spectra

All spectra shown (both static and time-resolved) were calculated at the DFT/MRCI level of theory using the aug-cc-pVDZ basis. We recently extended the DFT/MRCI method to calculate core-level excitation employing the core-valence separation (CVS) approximation, referred to
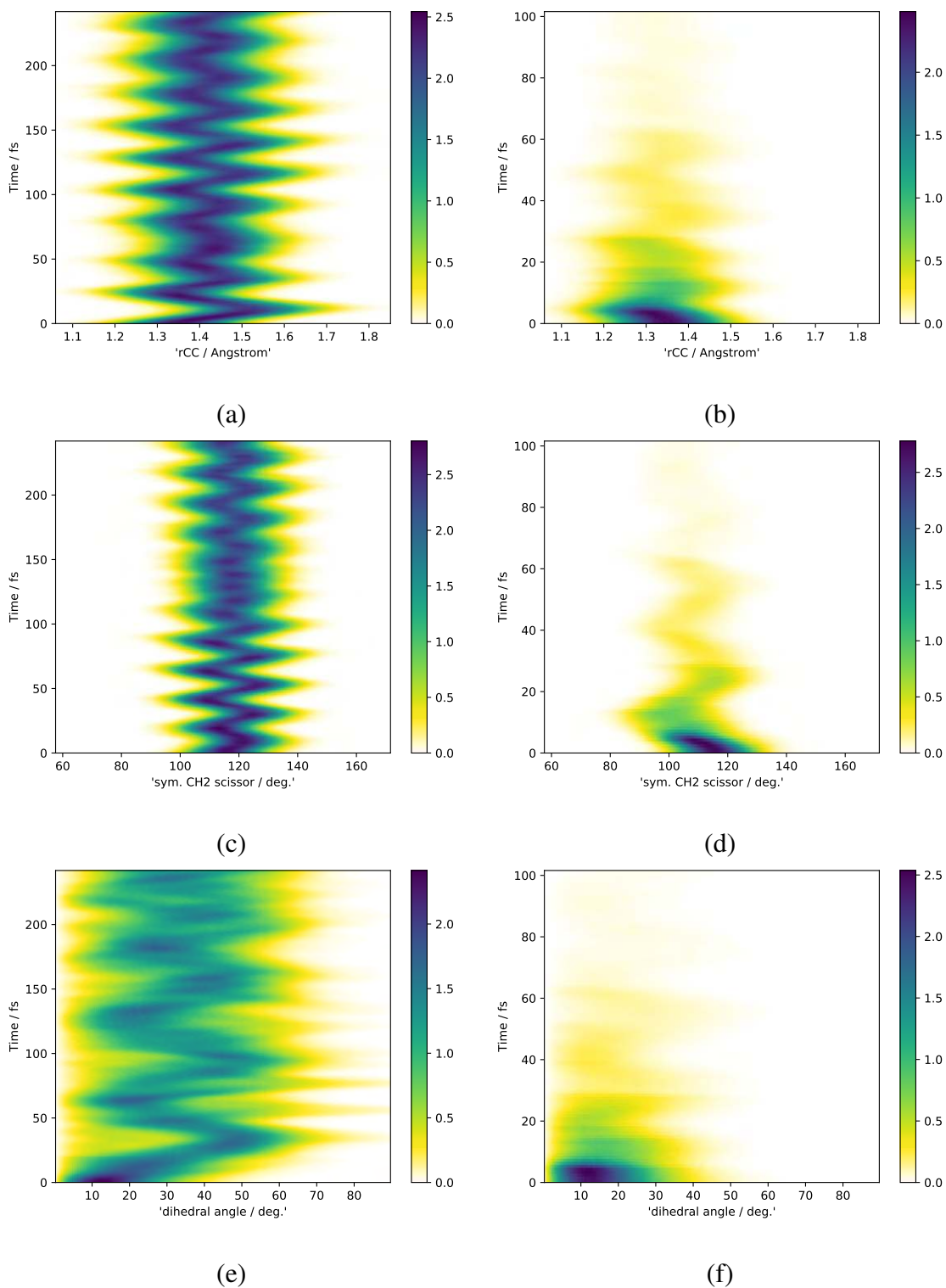
(a)

(b)

(c)

(d)

(e)

(f)

Figure S10: Reduced nuclear densities from AIMS simulations in which trajectory basis functions were initialized on D_0 (a), (c), (e) or D_1 (b), (d), (f). The densities shown correspond to the internal coordinates undergoing the largest-amplitude motions. Panels (a) and (c) denote the C=C stretch, (b) and (d) show the symmetric scissoring coordinates, and (e) and (f) evince the dihedral angle about the central C=C bond.

as CVS-DFT/MRCI (*37*). The simulated spectra, $\sigma(E)$, were computed as

$$\sigma(E) = H(\Delta E_{IP} - E)\frac{2E}{3}\left(\sum_I f_I \delta(E - \Delta E_I)\right) \otimes L(E; \Gamma) \tag{5}$$

where ΔE_I, f_I, and $H(\Delta E_{IP} - E)$ represent the CVS-DFT/MRCI core-excitation energies, oscillator strengths, and reverse Heaviside step function centered at the core ionization potential (ΔE_{IP}), respectively. $L(E; \Gamma)$ denotes a Gaussian lineshape with a FWHM Γ, which was set to 0.25 eV.

Static ground- and excited-state XAS are shown for the Franck-Condon (FC) point geometry, the D_0/D_1 minimum-energy conical intersection (MECI), and D_0 minimum geometry of ethylene, Figs. S11–S19.
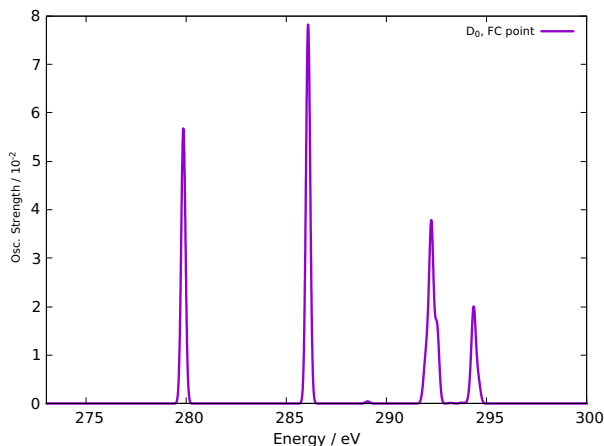

Figure S11: Calculated isotropic XAS for the D_0 state at the FC point using the CVS-DFT/MRCI/aug-cc-pVDZ level of theory.
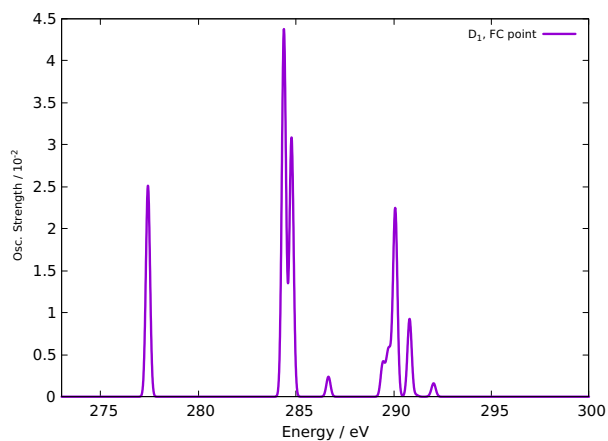
Figure S12: Calculated isotropic XAS for the D_1 state at the FC point using the CVS-DFT/MRCI/aug-cc-pVDZ level of theory.
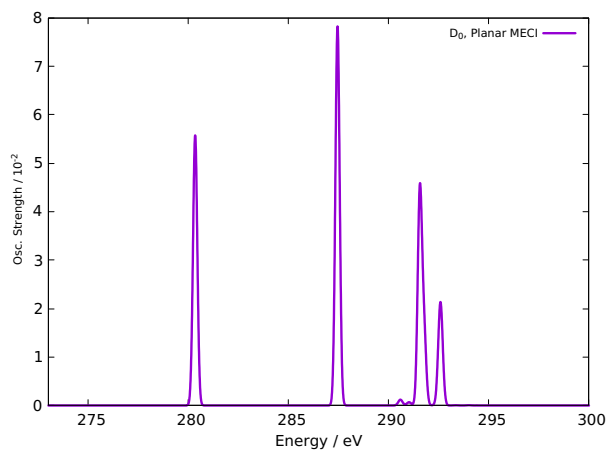

Figure S13: Calculated isotropic XAS for the D_0 state at the MECI geometry using the CVS-DFT/MRCI/aug-cc-pVDZ level of theory.
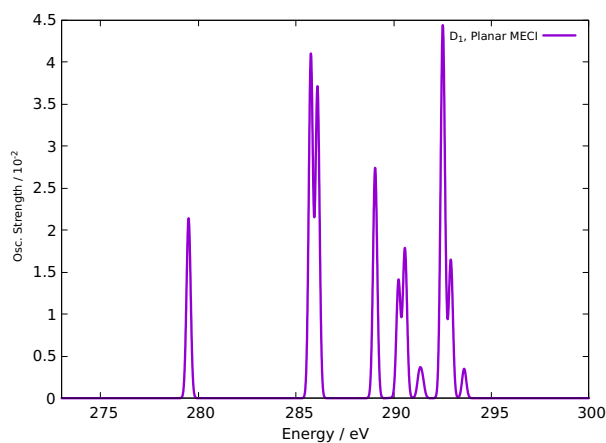
Figure S14: Calculated isotropic XAS for the D_1 state at the MECI geometry using the CVS-DFT/MRCI/aug-cc-pVDZ level of theory.
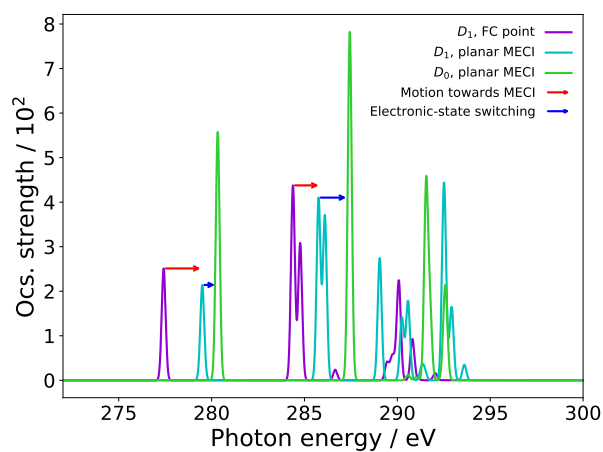

Figure S15: Calculated isotropic XAS for geometries and electronic states of interest. All calculations are performed at the CVS-DFT/MRCI/aug-cc-pVDZ level of theory.
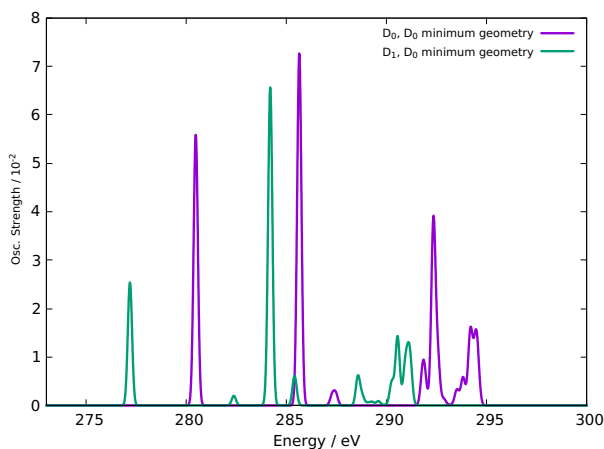
17

Figure S16: Calculated isotropic XAS for the D_0 and D_1 states at the D_0 minimum geometry. All calculations are performed at the CVS-DFT/MRCI/aug-cc-pVDZ level of theory.
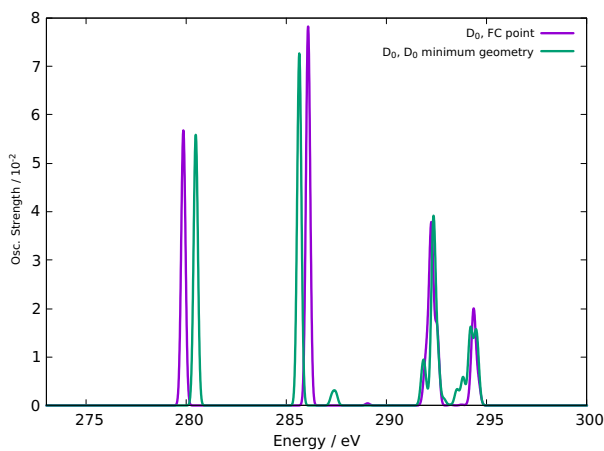

Figure S17: Calculated isotropic XAS for the D_0 state at both S_0 and D_0 minimum geometries. All calculations are performed at the CVS-DFT/MRCI/aug-cc-pVDZ level of theory.

Figure S18: Calculated isotropic XAS for the D_0 state at the D_0 minimum geometries, as well as the inner and outer turning points of the CC stretch vibration. All calculations are performed at the CVS-DFT/MRCI/aug-cc-pVDZ level of theory.
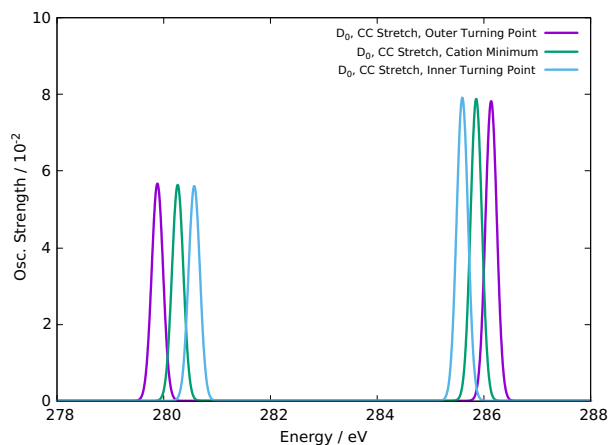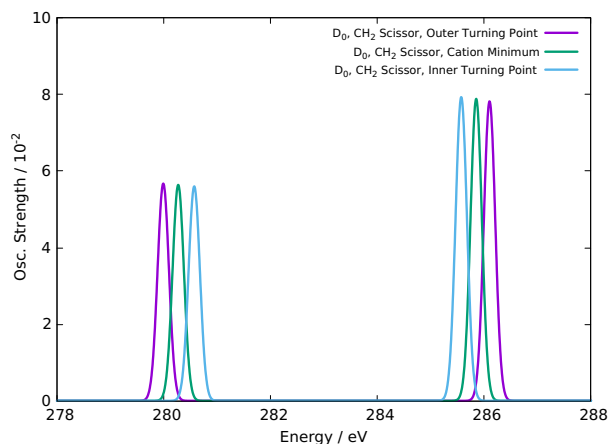

Figure S19: Calculated isotropic XAS for the D_0 state at the D_0 minimum geometries, as well as the inner and outer turning points of the CH_2 scissor vibration vibration. All calculations are performed at the CVS-DFT/MRCI/aug-cc-pVDZ level of theory.

S3.4 Theoretical ΔOD at different pump peak powers

The AIMS method used for TRXAS simulations shows the best agreement between theory and experiment at the highest peak intensity, 8.5×10^{14} W/cm^2, as shown in Figure S20**I**. In the experiment, the pump peak intensity is calculated for a Gaussian pulse in a Gaussian beam profile of 12 fs and is equal to 8.66×10^{14} W/cm^2.
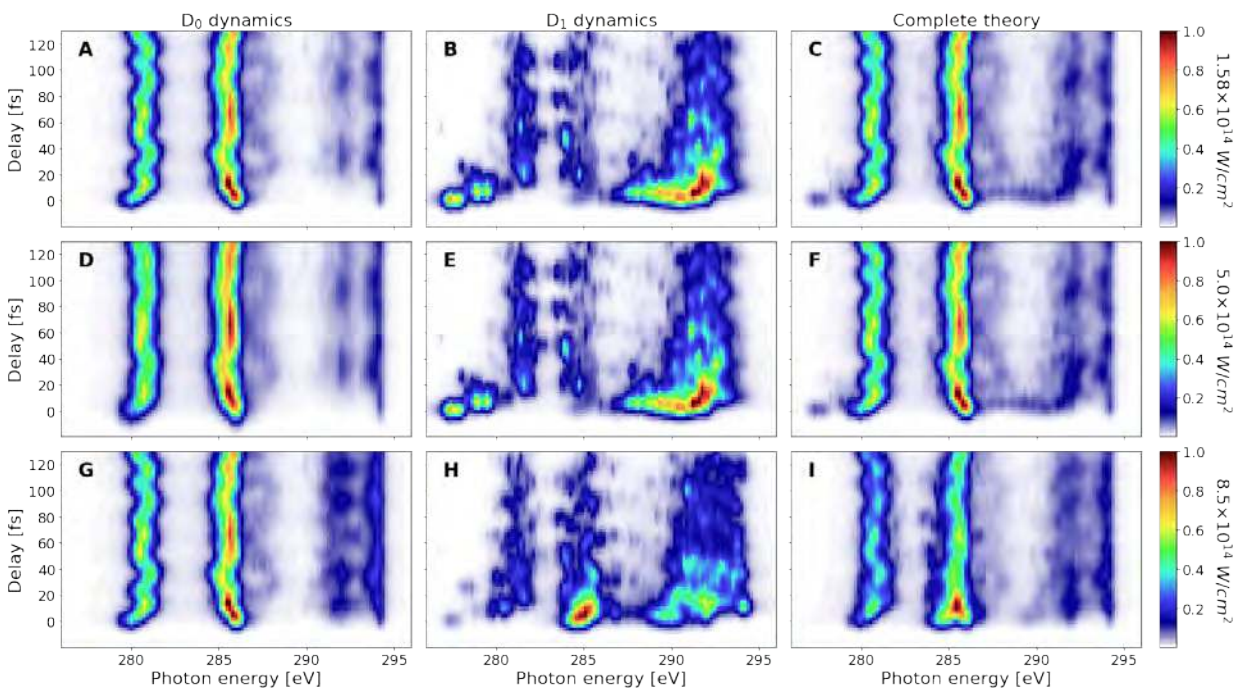

Figure S20: Normalized ΔOD spectra simulated with a distribution function and calculated at the different pump peak powers. D_0 (left), D_1 (middle), and combined (right) TRXAS spectra of ethylene cation at (**A, B, C**) 1.58×10^{14} W/cm^2, (**D, E, F**) 5.0×10^{14} W/cm^2, and (**G, H, I**) 8.5×10^{14} W/cm^2 peak intensities.

S4 Simulation of orientation-dependent strong-field-ionization yields

In the TRXAS simulations, the averaging over molecular orientations was achieved via the sampling of the orientation-dependent probability of strong-field ionization, $I(\theta, \varphi)$, where θ and ϕ denote, respectively, the polar and azimuthal angles between the laser-polarization and molecular axes. $I(\theta, \varphi)$ was computed at the time-dependent first-order algebraic diagrammatic construction (TD-ADC(1)) level of theory. In these calculations, an $\mathcal{L}^2$ Gaussian basis was employed, and a complex absorbing potential (CAP) was used to annihilate those components of the wave packet undergoing ionization. A brief description of this methodology and the specifics of the TD-ADC(1) calculations are given below.

S4.1 Time-dependent first-order algebraic diagrammatic construction

Let $|\mathrm{HF}\rangle$ denote the N-electron Hartree-Fock (HF) ground state. Let $\{\varphi_p(\boldsymbol{x})\}$ be the set of canonical HF orbitals with associated elementary Fermionic creation (annihilation) operators $\hat{a}_p^\dagger$ ($\hat{a}_p$). Here, we use $\boldsymbol{x}$ to denote the one-electron spin-spatial coordinates and $\boldsymbol{r}$ to denote the spatial coordinates alone.

The TD-ADC(1) wave packet $|\Psi(t)\rangle$ can be written as

$$
\begin{aligned}
|\Psi(t)\rangle &= \sum_{jb} C_{jb}(t)\hat{a}_j^\dagger \hat{a}_b |\mathrm{HF}\rangle . \\
&= \sum_{jb} C_{jb}(t) |\Phi_{jb}\rangle .
\end{aligned}
\tag{6}
$$

We note that the TD-ADC(1) wavefunction *ansatz* is identical to that of time-dependent configuration interaction singles (TD-CIS). The difference between the two methods lies, however, in that TD-ADC(1) uses modified transition dipoles, corresponding to a first-order perturbation theory correction to the CIS ones.

S4.2 The CAP-augmented Hamiltonian

Ignoring nuclear motion and adopting the dipole approximation, the interaction of the molecule with the applied laser pulse, $\boldsymbol{\epsilon}(t)$, was modeled using the Hamiltonian

$$\hat{H}(\boldsymbol{r}, t) = \hat{H}_{el}(\boldsymbol{r}) - \boldsymbol{\mu}(\boldsymbol{r}) \cdot \boldsymbol{\epsilon}(t). \tag{7}$$

Here, $\boldsymbol{r}$ denotes the electronic coordinates, $\hat{H}_{el}$ the field-free electronic Hamiltonian, and $\boldsymbol{\mu}$ the electronic component of the molecular dipole. To remove the components of the wave packet corresponding to the outgoing photoelectron, the Hamiltonian $\hat{H}(\boldsymbol{r}, t)$ is augmented with a CAP:

$$\hat{H}(\boldsymbol{r}, t) \rightarrow \tilde{H}(\boldsymbol{r}, t) = \hat{H}(\boldsymbol{r}, t) - i\hat{W}(\boldsymbol{r}). \tag{8}$$

Here, $\hat{W}(\boldsymbol{r})$ is a local, potential-type, one-electron operator that is non-zero only outside of the interaction region defined by the spatial extent of of the bound states of the system. The following monomial form was used for $\hat{W}$:

$$\hat{W}(\boldsymbol{r}; \eta, \boldsymbol{d}, n) = \eta \sum_{i=x,y,z} W_i(r_i; d_i, n), \tag{9}$$

$$W_i(r_i; d_i, n) = \begin{cases} 0, & |r_i| \leq d_i \\ (|r_i| - d_i)^n, & |r_i| > d_i. \end{cases} \tag{10}$$

Here, η denotes the CAP strength and n the CAP order, which together determine the rate at which the CAP increases outside of the interaction region. The parameters $\{d_i | i = x, y, z\}$ define a rectangular box containing within it the interaction region. An advantage of using a monomial-type CAP is that the molecular orbital (MO) matrix elements of this operator can be evaluated analytically when using Gaussian basis functions (*52*).

S4.3 Calculation of total ionization yields

Let $\Theta(\boldsymbol{r})$ be the characteristic function associated with the CAP box. That is, $\Theta(\boldsymbol{r})$ is equal to 1 for values of $\boldsymbol{r}$ within the CAP box (including the boundary) and is zero at all points outside of

the CAP box. Assuming that the CAP is parameterized properly, the integral of the flux, $F(t)$, passing into the CAP box will give the time-dependent probability of ionization, $P(t)$:

$$P(t) = \int_{-\infty}^{t} dt' F(t'). \tag{11}$$

In turn, the flux $F(t)$ can be calculated as the time-derivative of the expectation value of the characteristic function $\Theta(\boldsymbol{r})$:

$$\begin{aligned}
F(t) &= \frac{\partial}{\partial t} \langle \Psi(t)|\Theta(\boldsymbol{r})|\Psi(t)\rangle \\
&= i \left\langle \Psi(t) \left| \left[\hat{H}, \Theta(\boldsymbol{r})\right] \right| \Psi(t) \right\rangle.
\end{aligned} \tag{12}$$

S4.4 Channel-resolved ionization yields

Equation 12 defines the flux operator

$$\hat{F} = i \left[\hat{H}, \Theta(\boldsymbol{r})\right]. \tag{13}$$

The cation state-resolved fluxes $F_I(t)$, i.e., the flux going into the CAP region in a particular cation state $|\psi_I^{(N-1)}\rangle$, may be calculated as the expectation values of the projected flux operators

$$\hat{F}_I = \hat{\mathcal{P}}_I \hat{F} \hat{\mathcal{P}}_I, \tag{14}$$

where $\hat{\mathcal{P}}_I$ denotes the projector onto the Ith ADC(1) cation state. In the ADC(1) framework, ionization is described with a Koopmans' approximation-type picture. Thus, the cation states are simply given by $|\psi_I^{(N-1)}\rangle = \hat{a}_I|HF\rangle$, allowing the projector $\hat{\mathcal{P}}_I$ to be written as

$$\hat{\mathcal{P}}_I = \sum_a |\Phi_{Ia}\rangle \langle\Phi_{Ia}| \tag{15}$$

S4.5 Calculation details

S4.5.1 Basis set

The TD-ADC(1) calculations were performed using the aug-cc-pVDZ basis augmented with additional 5s, 5p, 5d and 5f diffuse functions of the Kauffman-Baumeister-Jungen type (*53*)

23

placed at the centre of mass.

S4.5.2 Laser pulse parameterization

The strong field pump pulse, $\boldsymbol{\epsilon}(t)$, was taken to assume the following functional form:

$$\boldsymbol{\epsilon}(t) = \boldsymbol{e}(\theta, \varphi) S_0 \sin\left(\omega\left[t - t_0\right]\right) \sin^2\left(\frac{\pi t}{2\Gamma}\right) h(t) h(2\Gamma - t). \tag{16}$$

Here, $\boldsymbol{e}(\theta, \varphi)$ denotes the laser polarization vector, ω is the central frequency, t_0 is the pulse centre, and Γ is the full width at half maximum (FHWM) of the pulse. S_0 denotes a strength parameter, and is used to set the peak intensity of the laser pulse. The step functions $h(t)$ and $h(2\Gamma - t)$ are used to force the laser pulse to zero at times $t < 0$ and $t > 2\Gamma$. The parameters used were $\omega = 0.0285$ a.u. (corresponding to a wavelength of 1600 nm), $\Gamma = 10$ fs, and $t_0 = 5$ fs. The strength parameter S_0 was set to yield peak intensities of 1.58×10^{14} Wcm^{-2}, 5.00×10^{14} Wcm^{-2}, and 8.50×10^{14} Wcm^{-2}.

S4.5.3 Solution of the time-dependent Schrödinger equation

The time-dependent Schrödinger equation was solved using the short iterative Lanczos-Arnoldi algorithm (*54*), and a total propagation time of 25 fs was used.

S4.5.4 CAP parameterization

The CAP box dimensions $\{d_x, d_y, d_z\}$ were determined automatically by searching for the points at which the ground state one-electron density falls below a threshold of 10^{-9} in each of the x-, y-, and z-directions, starting from the centre of mass of the molecule. This yielded CAP box parameters of $r_x = 15.9$ a.u., $r_y = 13.6$ a.u., and $r_z = 16.8$ a.u. The CAP strength, η, was set to 0.02, and a CAP order $n = 2$ was used. In order to minimise spurious interactions of the bound states with the CAP, the CAP operator was projected onto the space orthogonal to the ADC(1) states lying below the first-ionization potential (which is simply given by the negative of the HOMO energy in the ADC(1) framework).

S4.5.6 Orientation-dependent ionization yields

To utilise the orientation-dependent probabilities of strong-field ionization, $I(\theta, \varphi)$, in the simulation of the TRXAS, they need to be evaluated at arbitrary sampling points (θ_n, φ_n). To this end, $I(\theta, \varphi)$ was fitted to a multipole expansion in terms of the real spherical Harmonics $Y_{lm}(\theta, \varphi)$:

$$I(\theta, \varphi) \approx \sum_{l=0}^{l_{max}} \sum_{m=-l}^{l} A_{lm} Y_{lm}(\theta, \varphi). \tag{17}$$

A maximum expansion order $l_{max} = 10$ was used, and the multipole expansion coefficients A_{lm} were computed using the 194 point Lebedev quadrature scheme (*55, 56*).